

Multi-wavelength mid-infrared plasmonic antennas with single nanoscale focal point

Romain Blanchard,¹ Svetlana V. Boriskina,² Patrice Genevet,^{1,3} Mikhail A. Kats,¹ Jean-Philippe Tetienne,¹ Nanfang Yu,¹ Marlan O. Scully,³ Luca Dal Negro,⁴ and Federico Capasso^{1,*}

¹*School of Engineering and Applied Sciences, Harvard University, 9 Oxford Street, Cambridge, Massachusetts 02138, USA*

²*Department of Chemistry & The Photonics Center, Boston University, 590 Commonwealth Avenue, MA, 02215, USA*

³*Institute for Quantum Studies and Department of Physics, Texas A&M University, College Station, TX 77843, USA*

⁴*Department of Electrical and Computer Engineering, The Photonics Center & Division of Materials Science and Engineering Boston University, 8 St. Mary's St., Boston, MA, 02215, USA*

*capasso@seas.harvard.edu

Abstract: We propose and demonstrate a novel photonic-plasmonic antenna capable of confining electromagnetic radiation at several mid-infrared wavelengths to a single sub-wavelength spot. The structure relies on the coupling between the localized surface plasmon resonance of a bow-tie nanoantenna with the photonic modes of surrounding multi-periodic particle arrays. Far-field measurements of the transmission through the central bow-tie demonstrate the presence of Fano-like interference effects resulting from the interaction of the bow-tie antenna with the surrounding nanoparticle arrays. The near-field of the multi-wavelength antenna is imaged using an aperture-less near-field scanning optical microscope. This antenna is relevant for the development of near-field probes for nanoimaging, spectroscopy and biosensing.

©2011 Optical Society of America

OCIS codes: (240.6680) Surface plasmons; (260.3910) Metal optics; (250.5403) Plasmonics.

References and links

1. A. J. Huber, A. Ziegler, T. Köck, and R. Hillenbrand, "Infrared nanoscopy of strained semiconductors," *Nat. Nanotechnol.* **4**(3), 153–157 (2009).
2. J. M. Stiegler, A. J. Huber, S. L. Diedenhofen, J. Gómez Rivas, R. E. Algra, E. P. A. M. Bakkers, and R. Hillenbrand, "Nanoscale free-carrier profiling of individual semiconductor nanowires by infrared near-field nanoscopy," *Nano Lett.* **10**(4), 1387–1392 (2010).
3. F. Huth, M. Schnell, J. Wittborn, N. Ocelic, and R. Hillenbrand, "Infrared-spectroscopic nanoimaging with a thermal source," *Nat. Mater.* **10**(5), 352–356 (2011).
4. S. Kawata and Y. Inouye, "Scanning probe optical microscopy using a metallic probe tip," *Ultramicroscopy* **57**(2-3), 313–317 (1995).
5. B. Knoll and F. Keilmann, "Near-field probing of vibrational absorption for chemical microscopy," *Nature* **399**(6732), 134–137 (1999).
6. F. Zenhausern, Y. Martin, and H. K. Wickramasinghe, "Scanning interferometric apertureless microscopy: optical imaging at 10 angstrom resolution," *Science* **269**(5227), 1083–1085 (1995).
7. F. Keilmann and R. Hillenbrand, *Nano-Optics and Near-Field Optical Microscopy* (Artech House, 2008).
8. N. Ocelic, A. Huber, and R. Hillenbrand, "Pseudoheterodyne detection for background-free near-field spectroscopy," *Appl. Phys. Lett.* **89**(10), 101124 (2006).
9. M. Schnell, P. Alonso-Gonzalez, L. Arzubiaga, F. Casanova, L. E. Hueso, A. Chuvilin, and R. Hillenbrand, "Nanofocusing of mid-infrared energy with tapered transmission lines," *Nat. Photonics* **5**(5), 283–287 (2011).
10. F. De Angelis, G. Das, P. Candeloro, M. Patrini, M. Galli, A. Bek, M. Lazzarino, I. Maksymov, C. Liberale, L. C. Andreani, and E. Di Fabrizio, "Nanoscale chemical mapping using three-dimensional adiabatic compression of surface plasmon polaritons," *Nat. Nanotechnol.* **5**(1), 67–72 (2010).
11. S. V. Boriskina and L. Dal Negro, "Multiple-wavelength plasmonic nanoantennas," *Opt. Lett.* **35**(4), 538–540 (2010).
12. D. T. Schaafsma, R. Mossadegh, J. S. Sanghera, I. D. Aggarwal, J. M. Gilligan, N. H. Tolk, M. Luce, R. Generosi, P. Perfetti, A. Cricenti, and G. Margaritondo, "Singlemode chalcogenide fiber infrared SNOM probes," *Ultramicroscopy* **77**(1-2), 77–81 (1999).
13. S. Zou and G. C. Schatz, "Silver nanoparticle array structures that produce giant enhancements in electromagnetic fields," *Chem. Phys. Lett.* **403**(1-3), 62–67 (2005).

14. A. Gopinath, S. V. Boriskina, N.-N. Feng, B. M. Reinhard, and L. Dal Negro, "Photonic-plasmonic scattering resonances in deterministic aperiodic structures," *Nano Lett.* **8**(8), 2423–2431 (2008).
15. G. Vecchi, V. Giannini, and J. Gómez Rivas, "Shaping the fluorescent emission by lattice resonances in plasmonic crystals of nanoantennas," *Phys. Rev. Lett.* **102**(14), 146807 (2009).
16. Y. Chu, E. Schonbrun, T. Yang, and K. B. Crozier, "Experimental observation of narrow surface plasmon resonances in gold nanoparticle arrays," *Appl. Phys. Lett.* **93**(18), 181108 (2008).
17. A. Gopinath, S. V. Boriskina, B. M. Reinhard, and L. Dal Negro, "Deterministic aperiodic arrays of metal nanoparticles for surface-enhanced Raman scattering (SERS)," *Opt. Express* **17**(5), 3741–3753 (2009).
18. R. Adato, A. A. Yanik, J. J. Amsden, D. L. Kaplan, F. G. Omenetto, M. K. Hong, S. Erramilli, and H. Altug, "Ultra-sensitive vibrational spectroscopy of protein monolayers with plasmonic nanoantenna arrays," *Proc. Natl. Acad. Sci. U.S.A.* **106**(46), 19227–19232 (2009).
19. E. D. Palik, *Handbook of Optical Constants of Solids* (Academic press, 1991).
20. K. Kneipp, M. Moskovits, and H. Kneipp, *Surface-Enhanced Raman Scattering: Physics and Applications* (Springer, 2006).
21. K. T. Carron, W. Fluhr, M. Meier, A. Wokaun, and H. W. Lehmann, "Resonances of two-dimensional particle gratings in surface-enhanced Raman scattering," *J. Opt. Soc. Am. B* **3**(3), 430–440 (1986).
22. V. A. Markel, "Coupled-dipole approach to scattering of light from a one-dimensional periodic dipole structure," *J. Mod. Opt.* **40**(11), 2281–2291 (1993).
23. S. Zou, N. Janel, and G. C. Schatz, "Silver nanoparticle array structures that produce remarkably narrow plasmon lineshapes," *J. Chem. Phys.* **120**(23), 10871–10875 (2004).
24. F. J. García de Abajo, "Colloquium: Light scattering by particle and hole arrays," *Rev. Mod. Phys.* **79**(4), 1267–1290 (2007).
25. B. Auguie and W. L. Barnes, "Collective resonances in gold nanoparticle arrays," *Phys. Rev. Lett.* **101**(14), 143902 (2008).
26. P. Genevet, J.-P. Tetienne, E. Gatzogiannis, R. Blanchard, M. A. Kats, M. O. Scully, and F. Capasso, "Large enhancement of nonlinear optical phenomena by plasmonic nanocavity gratings," *Nano Lett.* **10**(12), 4880–4883 (2010).
27. A. Taflová and S. C. Hagness, *Computational Electrodynamics: the Finite-Difference Time-Domain Method*, 3rd ed. (Artech House, 2005).
28. B. M. Ross and L. P. Lee, "Comparison of near- and far-field measures for plasmon resonance of metallic nanoparticles," *Opt. Lett.* **34**(7), 896–898 (2009).
29. S. Zou and G. C. Schatz, "Narrow plasmonic/photonic extinction and scattering line shapes for one and two dimensional silver nanoparticle arrays," *J. Chem. Phys.* **121**(24), 12606–12612 (2004).
30. M. Schnell, A. Garcia Etxarri, A. J. Huber, K. B. Crozier, J. Aizpurua, and R. Hillenbrand, "Controlling the near-field oscillations of loaded plasmonic nanoantennas," *Nat. Photonics* **3**(5), 287–291 (2009).
31. N. Yu, E. Cubukcu, L. Diehl, M. A. Belkin, K. B. Crozier, D. Bour, S. Corzine, G. Höfler, and F. Capasso, "Plasmonic quantum cascade laser antenna," *Appl. Phys. Lett.* **91**(17), 173113 (2007).
32. R. Hillenbrand, B. Knoll, and F. Keilmann, "Pure optical contrast in scattering-type scanning near-field microscopy," *J. Microsc.* **202**(1), 77–83 (2001).
33. B. Knoll and F. Keilmann, "Enhanced dielectric contrast in scattering-type scanning near-field optical microscopy," *Opt. Commun.* **182**(4-6), 321–328 (2000).
34. R. Esteban, R. Vogelgesang, J. Dorfmueller, A. Dmitriev, C. Rockstuhl, C. Etrich, and K. Kern, "Direct near-field optical imaging of higher order plasmonic resonances," *Nano Lett.* **8**(10), 3155–3159 (2008).
35. M. Schnell, A. Garcia-Etxarri, A. J. Huber, K. B. Crozier, A. Borisov, J. Aizpurua, and R. Hillenbrand, "Amplitude- and phase-resolved near-field mapping of infrared antenna modes by transmission-mode scattering-type near-field microscopy," *J. Phys. Chem. C* **114**(16), 7341–7345 (2010).

1. Introduction

Infrared near-field imaging and spectroscopy are emerging as powerful tools for the understanding of the structure and chemistry of materials at the nanoscale. Recent notable examples include the infrared nanoscopy of strained semiconductors [1] and the nanoscale free-carrier profiling of semiconductor nanowires [2]. A major development in this field was a recent demonstration of infrared-spectroscopic nanoimaging using a thermal source [3]. The ability to use a spectrally broad source in such systems allows for the use of Fourier-transform infrared (FTIR) spectroscopy techniques at the nanoscale for the chemical identification of unknown nanostructures.

These applications typically rely on the use of scattering-type scanning near-field optical microscopy (s-SNOM) [4–7], where the diffraction limit is overcome by the use of a sharp atomic force microscope (AFM) tip acting as an antenna to concentrate the incident radiation to nanoscale volumes. By measuring the light scattered by the tip, one can obtain information on the local properties of a sample. One limit of this technique lies in the weakness of the tip-scattered field requiring complex detection schemes to isolate it from the strong background [8]. There is thus a need for more refined techniques to feed power into a nanoscale volume.

Recent examples of such techniques make use of tapered transmission lines [9] and adiabatic compression of surface plasmon polaritons [10].

We approach this technologically relevant problem by considering a novel optical antenna structure collecting radiation over an extended area and funneling it into a single well-defined nanoscale focal spot. Following a design strategy recently proposed for multi-wavelength plasmonic nanoantennas in the visible range [11], we present here a design based on embedding a single bow-tie nanoantenna in an array of scattering nanoparticles that funnel incident radiation into the central gap of the bow-tie. Moreover, we demonstrate the possibility to achieve multi-frequency operation by using nested particle arrays with multiple periodicities. Such multiple-wavelength single-focus structures implemented on the facet of a chalcogenide fiber [12] would enable the realization of a fiber-based multi-channel infrared scanning optical microscope by providing efficient focusing of the incident fiber-mode field into the nanoscale gap of the central bow-tie, while suppressing alignment sensitivity.

Moreover, differently from antenna arrays with periodic or aperiodic geometries featuring a high-density of hot-spots embedded in a background of photonic-plasmonic modes [13–18], the proposed single hot-spot structure benefits from enhanced spatial resolution due to the large contrast between the field enhancement at the gap of a bow-tie antenna and at the edges of the metallic nanoparticles surrounding the isolated hot-spot.

2. Photonic-plasmonic coupling

In order to describe the proposed design strategy, we first study a simplified design, as shown in Fig. 1(a), providing high field enhancement at only one selected wavelength. It relies on the use of a bow-tie antenna (shown in Fig. 1(b)) surrounded by straight single-periodic arrays of identical discs to concentrate light onto the bow-tie. The antenna performance is optimized for normal illumination by a plane wave linearly polarized along the bow-tie direction.

We used a commercial Fourier-transform time-domain (FDTD) package (Lumerical FDTD) to simulate the electromagnetic behavior of these structures. Throughout this paper, we will use the term field enhancement to refer to the quantity $|E|^2/|E_0|^2$, where E is the peak near-field amplitude of the electric field generated either in the center of the antenna gap in the case of the bow-tie, or in close proximity to the edge in the direction of the incident polarization in the case of the discs; normalized to the incident field intensity $|E_0|^2$. In all simulations, the structures are illuminated from the substrate side by a linearly-polarized plane wave.

The structures were designed to operate in the mid-infrared spectral region (free space wavelength $\lambda = 5\text{--}10\ \mu\text{m}$). Gold was chosen as a preferred material for the plasmonic elements because of its relatively low losses in that spectral range. Optical constants for gold used in the numerical simulations were taken from [19]. In all simulations and experiments the structures are located at an interface between a barium fluoride (BaF_2) substrate and air. BaF_2 was chosen as a substrate because it is transparent in the spectral region of interest and has a relatively low refractive index ($n \sim 1.42$) compared to other conventionally used mid-infrared materials (e.g. ZnSe $n \sim 2.4$, Ge $n \sim 4.0$, Si $n \sim 3.42$). A low refractive index is desirable in order to reduce dephasing effects between the waves propagating in air and those propagating in the substrate, since both concentrate energy onto the bow-tie antenna. Reduced dephasing effects result in sharper photonic-plasmonic resonances [20].

We followed a hierarchical approach to designing and optimizing this antenna, starting from tuning the local properties of individual plasmonic particles followed by the controlled assembly of these elements into ensembles whose scattering response is defined by their collective electromagnetic properties. For example, we maximized the amplitude of the field scattered by the array by overlapping the localized surface plasmon (LSP) resonance of each individual disc and the collective array resonance, because the scattering efficiency of each disc is maximized on resonance. This interplay between localized plasmonic resonances and array resonances has been discussed in much detail in the literature [13,16–18,21–25]. A similar concept of overlapping local and collective resonances was recently studied in the case

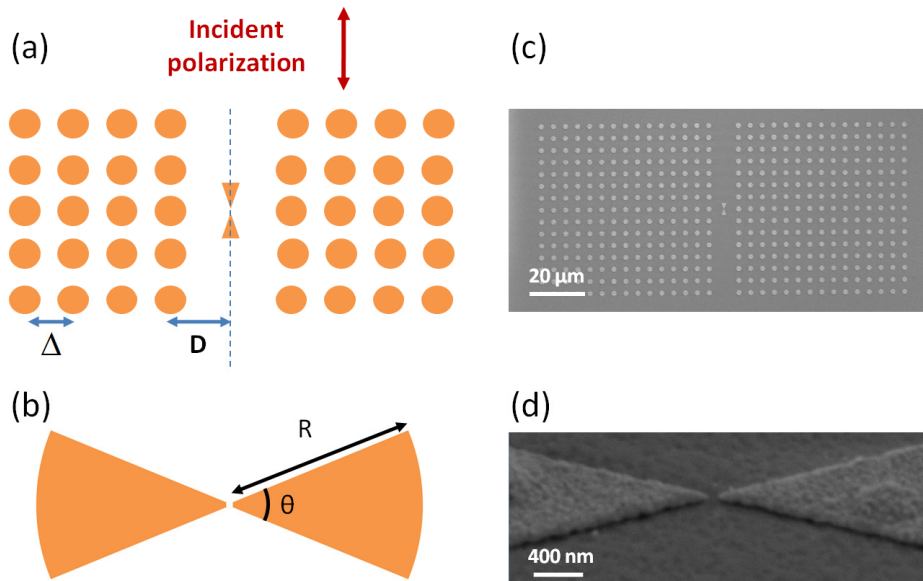


Fig. 1. (a) Schematic of a hybrid plasmonic-photonic antenna consisting of a bow-tie antenna surrounded by straight single-periodic arrays of identical discs. Light is assumed to be incident normal to the plane of the structure and with a polarization oriented vertically. The main parameters to be adjusted in the design are the discs diameter, the array periodicity Δ and the distance D between the arrays and the central bow-tie antenna. (b) Schematic of the gold bow-tie antenna considered in this work. It is composed of two sections of disc with radius $R = 2.2\mu\text{m}$ and $\theta = 45$ degrees opening angle. The central gap is 100 nm wide. (c) and (d) Scanning electron microscope (SEM) images of the fabricated structures. The gold discs have a radius of 890 nm. All structures have a thickness of 70 nm are deposited on a BaF_2 substrate. A zoom-in of the bow-tie gap is shown in (c).

of a plasmonic grating composed of deep resonant grooves [26]. However, we go further here and use these properties in complex non-uniform structures in order to engineer the near field excitation of particular selected elements.

Figure 2(a) shows the field enhancement of an isolated gold disc (in red) having a radius of 890 nm and a thickness of 70 nm. We observe a broad resonance with a maximum around $\lambda = 6.3\mu\text{m}$. For an infinite array of such discs, simulated by imposing periodic boundary conditions, we observe that for a period $\Delta = 4.3\mu\text{m}$ all the fields scattered by the discs add constructively in phase, leading to the existence of a relatively long lived photonic mode manifested as the sharp blue resonance on Fig. 2(a). In other words, the array of discs is designed to form a second order grating that couples incident radiation into an in-plane collective photonic mode. We emphasize that there is no propagating surface plasmon involved in this work. The different discs are only weakly coupled through their near-field since their separation is large compared to their diameter. They interact through their scattered fields, emitted into a dipolar-like emission pattern. Because almost no field is scattered in the direction of polarization of the incident light, while maximum scattering occurs in the direction normal to the incident wave polarization, the collective excitation of the discs result in waves propagating in the direction normal to the polarization of the incident light, where constructive interference of the scattered fields occurs [13]. This is different from a plasmonic grating composed of grooves, where propagating surface plasmons are launched in the direction of incident polarization.

The frequency spectrum of the calculated field enhancement in a gold bow-tie antenna is shown on Fig. 2(b). The geometrical parameters considered are detailed in the caption. For an isolated antenna under direct illumination by a plane wave, a broad resonance is observed,

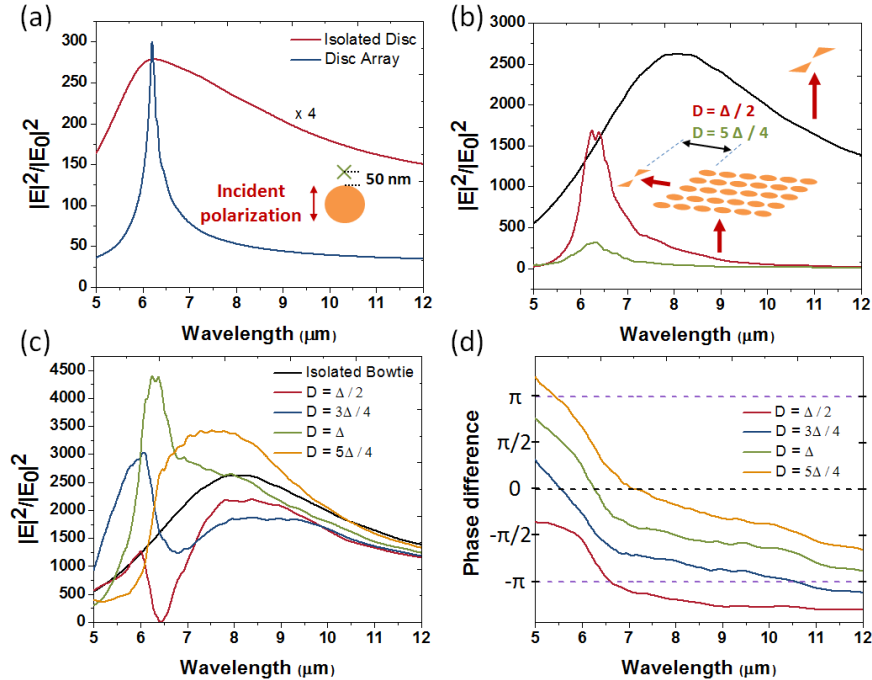


Fig. 2. (a) Simulated field enhancement for gold discs with 890 nm radius and 70 nm thickness at the interface between a BaF₂ substrate and air. In red, an isolated disc, with intensity magnified 4 times; in blue, an infinite two-dimensional array of such discs with periodicity $\Delta = 4.3 \mu\text{m}$. The near-field intensities are calculated 50 nm away from the disc edge, in the direction of the incident light polarization, as shown in the inset. We consider any arbitrary disc in the case of the infinite array as they are all equivalent. (b) Simulated field enhancement for a gold bow-tie antenna directly illuminated only by a plane wave (black) or illuminated only by the field scattered by the array of discs in (a), situated at a distance $D = \Delta/2$ (red) or $D = 5\Delta/4$ (green). The bow-tie is 70 nm-thick. Each arm is a section of disc with a radius of $2.2 \mu\text{m}$ and an opening angle of 45 degrees. The central gap is 100 nm wide. The insets represent the two excitation paths considered for the bow-tie antenna. (c) Simulated field enhancement at the center of the bow-tie gap, for an isolated bow-tie (black) and for the full structure as shown in Fig. 1(a), for different distances D between the bow-tie and the arrays of discs. (d) Phase differences between the two excitation paths of the bow-tie, as shown in the insets of (b), calculated at the center of the bow-tie gap, for different distances D between the bow-tie and the arrays of discs.

with a maximum at $\lambda = 8 \mu\text{m}$. Also shown on Fig. 2(b) is the field enhancement at the bow-tie gap when illuminated only by the field scattered by an array of discs similar to the one described above. As shown in the inset of Fig. 2(b), the plane wave in these latter simulations is incident only on the array while the bow-tie is illuminated only by the scattered field. This is made possible through the use of total-field/scattered-field boundaries [27] enclosing the array. We observe a large field enhancement corresponding to the scattering resonance of the array. Because of the diffraction of the scattered fields, the fields intensity at the bow-tie gap decreases with increasing distance between the array and the bow-tie (compare red and green curves).

We now assemble all these components to form the structure shown in Fig. 1(a). The two excitation paths for the bow-tie antenna, through direct illumination by the incoming plane wave (broad resonance), and through the fields scattered by the array of discs (relatively narrow resonance), give rise to a Fano-like interference phenomenon observed in the field intensity at the gap of the bow-tie antenna, as shown in Fig. 2(c). Depending on the distance D between the array and the bow-tie, and thus on the phase difference between the two excitation paths, either constructive or destructive interference occurs. In order to better

illustrate that phenomenon, we plot in Fig. 2(d) the phase difference between the two excitation paths, as observed at the center of the bow-tie, for different distances D . Horizontal lines indicate the particular values 0 , $-\pi$, and $+\pi$. As expected, whenever the phase difference vanishes, constructive interference occurs, leading to an increased intensity at the bow-tie gap. On the contrary, when the phase difference approaches $\pm\pi[2\pi]$, destructive interference is observed with a complete suppression of the bow-tie excitation in the case of $D = \Delta/2$.

We note that on Fig. 2(d), the curve corresponding to the shortest distance to the array (red) is not parallel to the other curves because evanescent components from the discs are still important at this point. We also observe that the phase difference is not exactly equal to π between two curves separated by $\Delta/2$. This translates the fact that as the scattered waves exit the array and propagate toward the bow-tie antenna, their effective wavelength changes. As a result, while the wavelength inside the array is equal to the periodicity Δ , so that the field scattered by two adjacent discs adds up in phase, this is no longer verified outside the array.

3. Fabrication and far-field characterization

We fabricated the structure shown in Fig. 1(a) and performed far-field measurements. As explained below, these measurements illustrate an indirect manifestation of the interference phenomena occurring in the near-field between the two excitation paths for the bow-tie antenna and confirm our understanding of the physical phenomena at play in the structures studied here.

Figure 1(c) and (d) shows scanning electron microscope (SEM) images of the structure represented in Fig. 1(a) and fabricated on a BaF_2 substrate using electron-beam (e-beam) lithography. As the substrate is electrically insulating, a thin layer (~ 6 nm) of chromium (Cr) was deposited using e-beam evaporation after photoresist (poly-methyl methacrylate) spinning. Following e-beam exposure, the Cr layer is etched away and the photoresist is developed. As the chromium etchant is in aqueous solution while BaF_2 is soluble in water, it is important to keep the etching time to a minimum. The gold patterns are then formed by e-beam evaporation of 70 nm of gold, followed by lift-off. As seen on Fig. 1(d), the gap of the bow-tie is well defined and has a width of ~ 90 nm. In the fabricated structures, the bow-tie antennas are each flanked by two arrays of discs arranged in a square lattice with period $\Delta = 4.3$ μm , and separated from the bow-tie by different distances D from $D = \Delta/2$ to $D = 5\Delta/4$. The arrays contain 15×15 discs each.

The far-field measurement setup is presented in Fig. 3 and consists of a Bruker Fourier-transform infrared (FTIR) spectrometer connected to an infrared microscope (containing only reflective optics). A particularity of the setup is the use of a knife-edge aperture inserted in a plane conjugate to the sample plane, which enables us to measure the far-field radiated from a specific rectangular area of the sample. Here we use it to measure the far-field radiated from a $6\mu\text{m} \times 9.5\mu\text{m}$ area enclosing the central bow-tie antenna.

Figure 4 shows the simulated transmission spectrum (red) through a single isolated bow-tie antenna, similar to the one described above. We observe a well-defined transmission dip at $\lambda \sim 7.2$ μm . One could expect the transmission dip to be closer to the near-field intensity maximum ($\lambda \sim 8$ μm), because this is where the material absorption and in-plane scattering are maximized. However, for the particular antenna design and the frequency range studied here, the dominant phenomenon explaining the transmission dip is the destructive interference between the directly transmitted light and the light scattered by the bow-tie. The position of maximum destructive interference, and hence of the transmission dip, is blue-shifted with respect to the near-field resonance for two main reasons: first the phase difference of the scattered field with respect to the incident field gets closer to π on the high-frequency side of the intensity resonance and second, the amplitude of the scattered field is expected to be peaked on the blue-side of the near-field peak [28]. The precise position of the transmission dip results from an interplay between phase and amplitude of the scattered light and directly transmitted light.

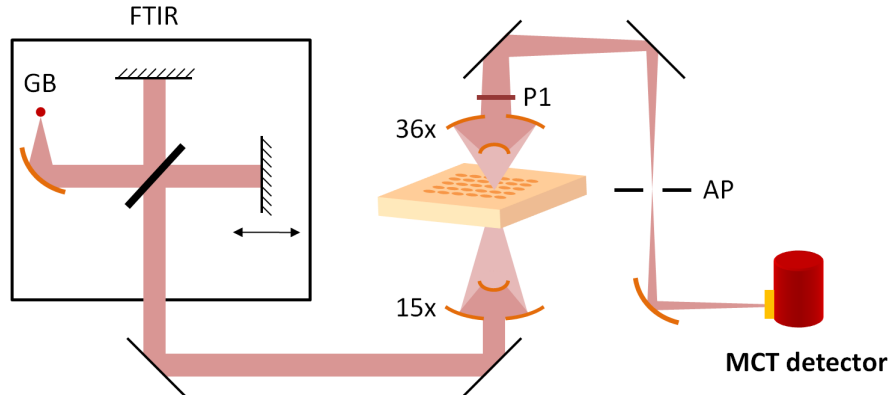


Fig. 3. Schematic of the far-field characterization setup composed of a Bruker Vertex 70 FTIR spectrometer equipped with a Bruker Hyperion 2000 FTIR-microscope. The source of light is a globar (GB). One arm of the interferometer is focused on the sample with a 15x reflective (Cassegrain) objective (NA 0.4) and the transmitted/scattered light is collected with a 36x reflective objective (NA 0.5). A polarizer (P1) is inserted in the beam path. Light is then re-focused and a knife-edge aperture (AP) is inserted in the image plane to select only the light coming from a specific area. Finally, light is focused onto a liquid nitrogen cooled MCT detector. Not represented in the schematic are a set of two movable mirrors which introduce visible white light and extract a visible output toward a set of binoculars. This visible beam, overlapped with the infrared beam, enables the alignment and focusing of the sample. As the signal detected by the MCT is very small, special care is taken to obtain significant spectra. For all measurements, the spectra are averaged over 256 scans and we use a low scan speed ($1\text{mm}\cdot\text{s}^{-1}$) for the scanning mirror of the FTIR, in order to have more integration time on the detector for each point. We extract the signal from the MCT detector after its dedicated pre-amplifier and use a second external voltage pre-amplifier (20x) with a low-pass filter at 1 kHz. A low-pass Butterworth filter is applied on the final spectra to remove the high frequency noise and smoothen the curves.

Also shown in Fig. 4 is the measured transmission spectrum (blue). Here, as in all our measurements (see Fig. 5), the transmission dips are systematically blue-shifted by $\sim 10\%$ of their expected position. We believe this blue shift stems from imperfect modeling of the frequency-dependent optical constants of the various materials in our system. The experimental transmission dip is shallower and broader than the simulated one, which we believe is mainly due to the fact that our illumination is not a plane wave, as in the simulations, but a focused beam collected with an objective having a finite numerical aperture.

All measured and simulated transmission curves are normalized to the transmission obtained for the incident light polarized perpendicularly to the antenna axis. This enables us to extract more selectively the part of the transmission that results from the interaction with the fields scattered by the bow-tie antenna near its LSP resonance. In particular, as shown in the inset of Fig. 5 (a), the aperture over which transmission is measured (red frame) may include some discs at small distances D between the bow-tie and the arrays. Transmission through this aperture thus also contains information on the interaction of the fields scattered by the discs with the directly transmitted light. Using the fact that the scattering properties of the discs are polarization insensitive, our normalization scheme enables to extract the transmission properties of the bow-tie antenna. We note that we cannot use, as an alternative solution, a smaller aperture in our experimental setup because the intensity impinging on the MCT detector would then be too low.

We now use the fact that the transmission dip results from an interference phenomenon to obtain information about the near-field intensity at the gap of the bow-tie through far-field measurements. Indeed, when the arrays of discs contribute to a stronger excitation of the bow-tie, the fields scattered by the bow-tie will be larger and thus the destructive interference will be stronger, resulting in a more pronounced transmission dip. On the contrary, when

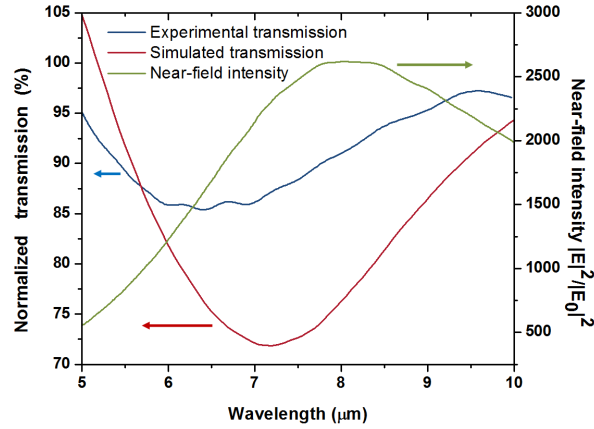


Fig. 4. Simulated (red) and measured (blue) normalized transmission through a $6 \mu\text{m} \times 9.5 \mu\text{m}$ area enclosing an isolated bow-tie antenna. The transmission curves are normalized to that obtained for the incident light polarized perpendicularly to the antenna axis. A rectangular monitor positioned 500 nm above the bow-tie and having the same dimensions as the knife-edge aperture is used in the simulation to calculate the transmission. (green) Simulated near field enhancement at the central gap of an isolated bow-tie antenna.

destructive interference occurs between the two excitation paths of the bow-tie, the intensity of the scattered light will be suppressed and a larger transmission is expected. These effects are clearly observed in the results of the simulations shown in Fig. 5(a), in reasonable agreement with the experimental spectra shown in Fig. 5(b).

The curves shown on Fig. 5 represent the ratio between the normalized transmission of the bow-tie embedded in the arrays of discs and the normalized transmission of an isolated bow-tie:

$$T_{ratio} = \frac{T_{embedded}^N}{T_{isolated}^N} = \frac{T_{embedded}^{\perp}}{T_{embedded}^{\parallel}} \bigg/ \frac{T_{isolated}^{\perp}}{T_{isolated}^{\parallel}},$$

where T_i^N is the normalized transmission, T_i denotes the transmission obtained for light polarized along the bow-tie antenna axis and T_i^{\perp} the transmission obtained for light polarized perpendicularly to the bow-tie axis.

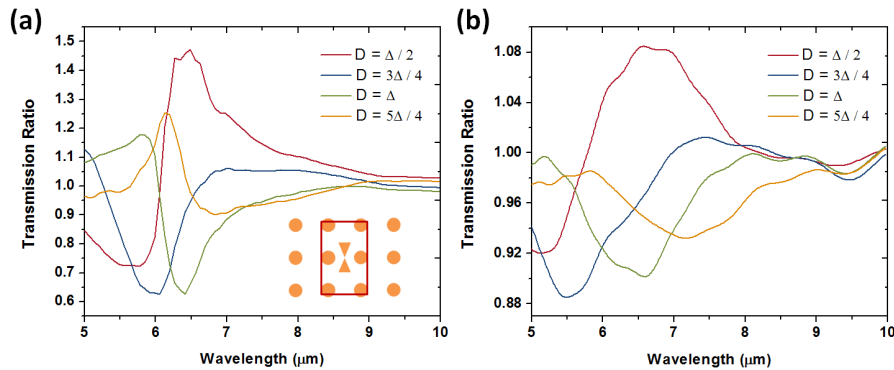


Fig. 5. (a) Simulated transmission ratio for different distances D between the bow-tie and the arrays of discs. The reference is an isolated bow-tie antenna. The inset is a schematic representing the size of the aperture (red frame) with respect to the structure. Shown here is the case $D = \Delta / 2$. (b) Experimental transmission ratio for different distances D between the bow-tie and the arrays of discs.

We observe a reasonable agreement between simulations and experiments. As discussed above, the experimental features are broader, shallower and systematically blue-shifted. Compared to the case of an isolated bow-tie antenna, an additional factor contributes here to the increased width of the measured spectral features. Because the beam waist illuminating the sample has a diameter of $\sim 20\mu\text{m}$, only a few periods of the arrays are illuminated, leading to a broadening of the corresponding spectral features. As the distance D between the bow-tie and the arrays increases, the illuminated portion of the arrays decreases in size, resulting in the decreased depth and increased width of the measured spectral features observed in Fig. 5(b). Previous theoretical simulations of single-periodic grating-assisted antennas revealed that they are robust to disorder with random displacements of the particles up to 30% of the lattice spacing [29]. We thus do not expect fabrication-induced disorder to be contributing significantly to the observed discrepancies between experiments and simulations.

The measurements clearly show the existence of both dips and peaks in the transmission spectra, corresponding to either increased or decreased near-field excitation of the central bow-tie. They thus constitute a demonstration of the interference occurring between the two excitation paths for the bow-tie antenna. Furthermore, they confirm that the transmission dip observed is mainly the result of an interference phenomenon between the directly transmitted light and the light scattered by the bow-tie. In particular, the observed suppressed transmission caused by the presence of the arrays around the bow-tie can only be explained by the mechanism of destructive interference.

4. Multi-wavelength antenna and near-field imaging

Having experimentally proven the possibility of engineering and manipulating the coupling between the LSP resonance of the bow-tie antenna and the collective photonic-plasmonic resonance of the disc array, we proceed to design a more complex triple-band antenna, as shown in Fig. 6(a). It relies on the use of a single bow-tie antenna to provide a high field enhancement at its central gap, surrounded by arrays of discs with three different periodicities and disc diameters to concentrate light onto the bow-tie at three selected wavelengths. The arrays are arranged radially, thereby reducing the polarization sensitivity of the structure and making efficient use of the space surrounding the bow-tie antenna. The geometrical parameters of the structure are detailed in the caption of Fig. 6. We noticed in our simulations that the disc LSP resonance match with the collective array resonance when the disc diameter is roughly equal to half the array periodicity. Considering the large width of the discs LSP

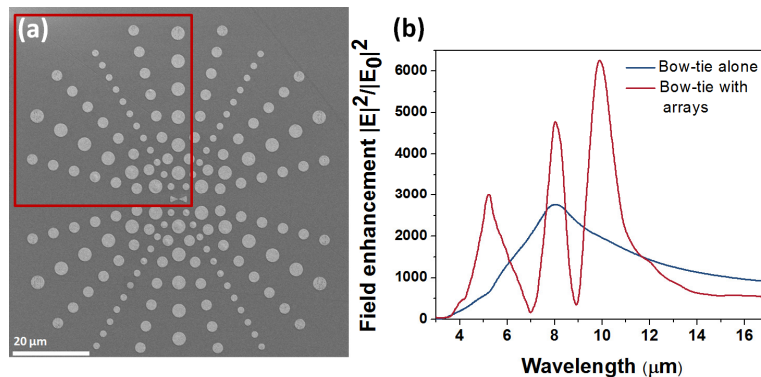


Fig. 6. (a) SEM image of the fabricated triple-band antenna. The red frame indicates the area over which the near-field image in Fig. 8 is taken. The arrays periodicities are $3.6\ \mu\text{m}$, $5.7\ \mu\text{m}$ and $7.2\ \mu\text{m}$. The corresponding discs diameters are respectively $1.8\ \mu\text{m}$, $2.85\ \mu\text{m}$ and $3.6\ \mu\text{m}$, and the distances between the bow-tie gap and the center of the first disc are respectively $3.6\ \mu\text{m}$, $11.4\ \mu\text{m}$ and $7.2\ \mu\text{m}$. The bow-tie is composed of two sections of disc with radius $2.2\ \mu\text{m}$ and 45 degrees opening angle. The central gap is $100\ \text{nm}$ wide. All structures have a thickness of $70\ \text{nm}$ and are deposited on a BaF_2 substrate. (b) Simulated field enhancement at the center of the bow-tie for the structure shown in (a) (red) and for an isolated bow-tie (blue).

resonance, we chose this simple rule to design our structure. The distance between the bow-tie gap and the center of the first disc for each array is equal to an integer multiple of the array periodicity, in order to obtain constructive interference, as seen above. We note that in this work we use a bow-tie antenna as the central element, but any structure featuring a high near-field enhancement due to an LSP resonance could be used instead. In particular, replacing a bow-tie with a sharp metallic tip could provide a high field-enhancement in a volume that is more accessible to a sample to be measured [10].

We show in Fig. 6(b) the field enhancement obtained at the center of the bow-tie. We observe that at the three wavelengths corresponding to the scattering resonances of the three different arrays, the field enhancement in the bow-tie gap is increased as compared to that in the isolated bow-tie (blue). Additionally, we observe that intensity is strongly suppressed in between the enhanced peaks due to the destructive interference mechanism discussed above. We note that the three wavelengths of operation of our device are spanning more than one octave, which could open interesting applications using non-linear processes such as second-harmonic generation.

We imaged the near-field supported by the structure using the mid-infrared transmission-mode s-SNOM setup represented in Fig. 7. Transmission-mode s-SNOM [30] is used to minimize near-field distortions by the probing tip and to provide a homogeneous illumination. The s-SNOM setup is based on a commercial atomic force microscope (AFM) (PSIA XE-120), previously used in [31]. The beam of a continuous-wave 10W CO₂ laser emitting at $\lambda = 10.6 \mu\text{m}$ is first expanded (for safety reason) and then focused onto the sample, after significant atmospheric absorption. This attenuation is desirable because our source is too powerful and could otherwise damage the sample. The ZnSe lens used to focus the beam on the sample is chosen so that the focus size is on the order of the size of our antenna structure ($\sim 100 \mu\text{m}$). A metal-coated AFM tip (Mikromash NSC19/Pt/AIBS) with resonant frequency $\sim 90 \text{ kHz}$ is then scanned over the sample in tapping mode, scattering the near-field into free-space propagating radiation collected by a set of ZnSe lenses and focused onto a liquid-nitrogen cooled Mercury-Cadmium-Telluride (MCT) detector. Lock-in detection at the second harmonic of the tapping frequency of the AFM tip was utilized to discriminate the scattered

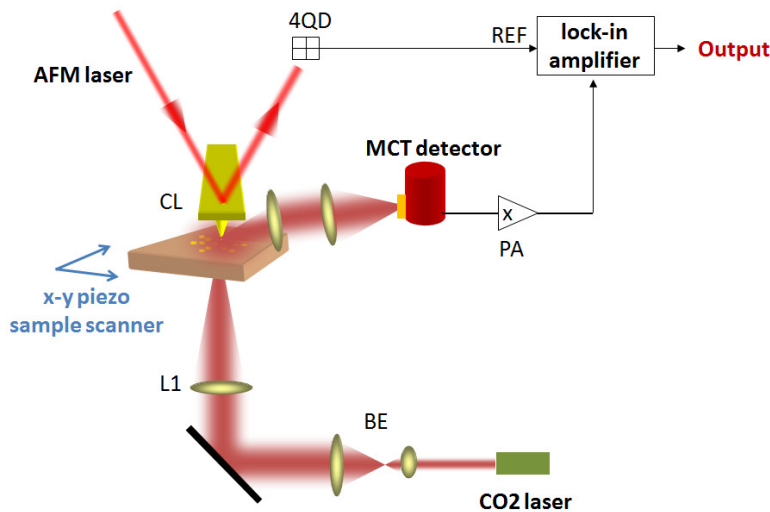


Fig. 7. Schematic of the transmission mode s-SNOM used to image the near-field around the antenna. BE is a beam expander composed of two ZnSe lenses with respective focal lengths 0.5" and 2". L1 is a long focal length (3") ZnSe lens, focusing the beam onto a $\sim 100\mu\text{m}$ -diameter spot. CL is the AFM cantilever and tip. 4QD is the four-quadrant detector of the AFM monitoring the oscillation of the AFM tip. We used it as the reference signal for the lock-in amplifier. PA is the pre-amplifier of the liquid nitrogen cooled MCT detector.

near-fields from the optical background that originated mainly from reflection and scattering of laser light from the tip shaft, the cantilever end, and the structure itself [32,33].

Figure 8 shows the measured SNOM signal as well as the FDTD simulation of the E_z component (perpendicular to the sample plane) of the electric field taken 10 nm above the gold structures. Only one quadrant is shown, corresponding to the red frame in Fig. 6(b), as information on the other quadrants is deduced by simple symmetry considerations. As expected, our metallic tip is sensitive mainly to the normal component of the electric fields (E_z). A large elastic scattering background can be seen in our SNOM image. It is both an amplitude background, resulting in the diffuse bright spots spreading over the structure, and a phase background, resulting in the distortions of the measured near-field pattern. For example, the intensity minima crossing the discs are not always aligned along the vertical diameter but can be tilted and shifted because of interference between the scattered near-field and the background scattering [33]. Background suppression methods such as cross-polarization schemes [34] and pseudo-heterodyne detection [8] can be employed to reduce this spurious background which contains no useful information on the near-field distribution. However, as discussed in [35] even the state-of-the-art s-SNOM setups including all these background suppression techniques still suffer from these background issues. Considering the large dimensions of our scanning areas, the problem is even more serious and would require the development of novel techniques that are outside the scope of this paper.

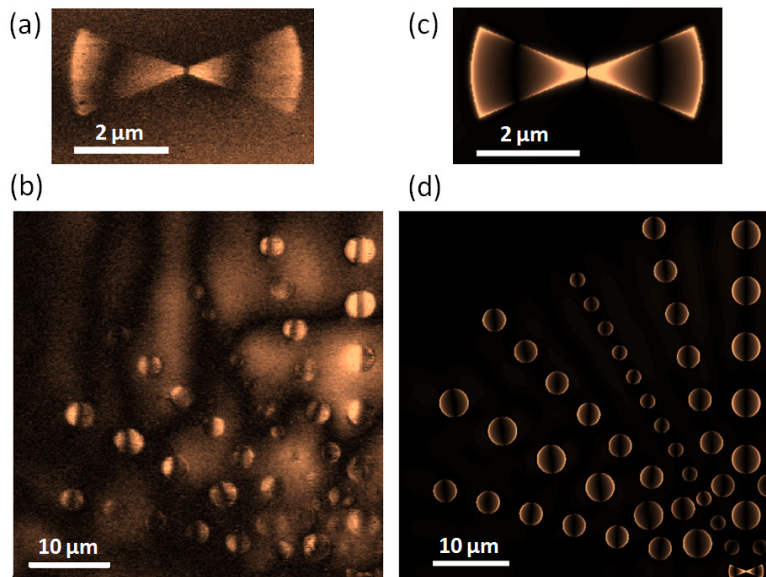


Fig. 8. (a) and (b) Experimental near-field images of the fabricated antenna shown in Fig. 6(a). (c) and (d) Simulated E_z -component of the near-field monitored 10 nm above the gold structures.

However, the main features of the simulation are visible in the experimental data. Each disc has two high intensity lobes diametrically opposed in the direction of incident polarization, separated by an intensity minimum. The arrays with the largest discs, having a resonance frequency around $\lambda = 10 \mu\text{m}$, are maximally excited, while the arrays of smaller discs remain relatively dark. The field-enhancement contrast between the discs and the central bow-tie is not visible in Fig. 8, because only the E_z -component of the electric field is shown for the simulation results and our experiment mainly measures that same field component, while the stronger field component at the bow-tie gap is in-plane. Simulations indicate that when the total intensity is taken into account, the bow-tie gap is one to two orders of magnitude brighter than the discs edges. The structures thus conserve a high spatial resolution.

Importantly, the multi-band capabilities of our design opens the possibility to further increase the spatial resolution using nonlinear effects, since the central bow-tie gap is the only spot with high enhancement at multiple wavelengths. A sensing scheme relying on the simultaneous near-field enhancement of several wavelengths in a single nanoscale volume could be implemented using our antenna. More generally, plasmonic antennas capable of focusing light into a single sub-wavelength spot at multiple frequencies, potentially spanning more than one octave as shown here, can be used for a range of novel functions, including the resonant enhancement of both pumping and emission efficiency of nanoscale emitters, background-free sensing of optically trapped nanoparticles, broadband near-field imaging, Raman and fluorescence sensing of multiple molecular targets with nanoscale spatial resolution [11].

5. Conclusion

We have proposed and demonstrated a new antenna structure that provides high electric field enhancement at multiple wavelengths in a single nanoscale focal point. The structure uses the coupling between the LSP resonance of a central bow-tie antenna and the photonic-plasmonic modes of an array of resonant nanoparticles. A simplified design providing a high field enhancement at one selected wavelength was used to study this coupling, through FDTD simulations and far-field transmission experiments. Calculations and experiments confirmed the existence of Fano-like interference phenomena between the two excitation paths of the bow-tie, through direct illumination and through illumination by the scattered field of the surrounding nanoparticle arrays. The near-field of the proposed structures has been imaged using an s-SNOM setup, and the experimental data confirmed the possibility of simultaneous excitation of both the arrays photonic resonances and the central bow-tie nanoantenna. The work presented here gives insight into the interactions between local and collective plasmonic or photonic modes of complex antenna structures and paves the road to the development of broadband nanoantennas with high-spatial resolution that can be utilized as near-field probes for a variety of applications in nanoimaging, spectroscopy and biosensing.

Acknowledgments

We thank Kenneth B. Crozier for access to his laboratory and the AFM used for s-SNOM setup. We thank Paul Steinvurzel for his help with the s-SNOM setup and helpful discussions. We acknowledge support from the Harvard Nanoscale Science and Engineering Center. This work was performed in part at the Center for Nanoscale Systems at Harvard University, a member of the National Nanotechnology Infrastructure Network, which is supported by the National Science Foundation (NSF). The computations in this paper were run on the Odyssey cluster supported by the FAS Science Division Research Computing Group at Harvard University. MOS and PG acknowledge NSF Grant No. EEC-0540832 (MIRTHE ERC), the Office of Naval Research, and the Robert A. Welch Foundation (A-1261). MAK is supported by the NSF through a Graduate Research Fellowship. JPT is supported by the École Normale Supérieure de Cachan, France. LDN acknowledges support from the Air Force program “Deterministic Aperiodic Structures for On-chip Nanophotonic and Nanoplasmonic Device Applications” under Award FA9550-10-1-0019, and from the NSF Career Award ECCS-0846651. SVB acknowledges support from the EU COST Action MP0702 “Towards functional sub-wavelength photonic structures”.